CHEMISTRY
A EUROPEAN JOURNAL

DOI: 10.1002/chem.201000458

Structural and Electronic Effects of Carbon-Supported Pt_xPd_{1-x} Nanoparticles on the Electrocatalytic Activity of the Oxygen-Reduction Reaction and on Methanol Tolerance

Shih-Hong Chang,[a] Wei-Nien Su,[a] Min-Hsin Yeh,[a] Chun-Jern Pan,[a] Kuan-Li Yu,[b] Din-Goa Liu,[b] Jyh-Fu Lee,[b] and Bing-Joe Hwang*[a, b]

Abstract: We report a systematic investigation on the structural and electronic effects of carbon-supported Pt_xPd_{1-x} bimetallic nanoparticles on the oxygen reduction reaction (ORR) and methanol oxidation reaction (MOR) in acid electrolyte. Pt_xPd_{1-x}/C nanocatalysts with various Pt/Pd atomic ratios ($x=$ 0.25, 0.5, and 0.75) were synthesized by using a borohydride-reduction method. Rotating-disk electrode measurements revealed that the Pt_3Pd_1/C nanocatalyst has a synergistic effect on the ORR, showing 50% enhancement, and an antagonistic effect on the MOR, showing 90% reduction, relative to JM 20 Pt/C on a mass basis. The extent of alloying and Pt d-band vacancies of the Pt_xPd_{1-x}/C nanocatalysts were explored by extended X-ray absorption fine-structure spectroscopy (EXAFS) and X-ray absorption near-edge structure spectroscopy (XANES). The structure–activity relationship indicates that ORR activity and methanol tolerance of the nanocatalysts strongly depend on their extent of alloying and d-band vacancies. The optimal composition for enhanced ORR activity is Pt_3Pd_1/C, with high extent of alloying and low Pt d-band vacancies, owing to favorable O–O scission and inhibited formation of oxygenated intermediates. MOR activity also shows structure dependence. For example, Pt_1Pd_3/C with $Pt_{rich-core}Pd_{rich-shell}$ structure possesses lower MOR activity than the Pt_3Pd_1/C nanocatalyst with random alloy structure. Herein, extent of alloying and d-band vacancies reveal new insights into the synergistic and antagonistic effects of the Pt_xPd_{1-x}/C nanocatalysts on surface reactivity.

Keywords: fuel cells · nanoparticles · oxygen reduction reaction · palladium · platinum

Introduction

The commercialization of fuel cells, either hydrogen or methanol fed, as clean-energy conversion devices largely depends on the development of stable and reliable electrocatalysts. Voltage losses result from poor electrochemical kinetics at both the anodes and cathodes of H_2- and CH_3OH-fed fuel cells.[1–4] The situation is even worse if methanol crosses over from the anode to the cathode side.[5,6] The competition between oxygen reduction and methanol oxidation reactions on traditional Pt electrocatalysts causes unfavorable overpotential for the oxygen reduction reaction (ORR), and the cathode efficiency decreases.[7–9] A further main factor responsible for the kinetic limitations associated with the cathode electrocatalyst in direct methanol fuel cells (DMFCs) originates from the high energy barrier of dioxygen dissociation and from the chemisorption of various oxygenated intermediates at the active site of the electrocatalyst.[10] These issues are believed to be responsible for the reduced efficiency of DMFCs.

One ambitious approach to solving the above-mentioned problems is to develop Pt-based bimetallic electrocatalysts with enhanced functionality to achieve superior ORR activity and methanol tolerance. Recently, significant progress has been made towards understanding the role of surface chemistry and electronic structures of Pt-based alloy surfaces[11–13] and nanoparticles.[14] The correlation between the d-

[a] Dr. S.-H. Chang, Dr. W.-N. Su, Dr. M.-H. Yeh, Dr. C.-J. Pan, Prof. B.-J. Hwang
Department of Chemical Engineering
National Taiwan University of Science and Technology
#43, Sec.4, Keelung Rd., Taipei, 10607, Taiwan (R.O.C.)
E-mail: bjh@mail.ntust.edu.tw

[b] Dr. K.-L. Yu, D.-G. Liu, Dr. J.-F. Lee, Prof. B.-J. Hwang
National Synchrotron Radiation Research Center
101 Hsin-Ann Road, Hsinchu Science Park
Hsinchu 30076, Taiwan (R.O.C.)
E-mail: jflee@nsrrc.org.tw

Supporting information for this article is available on the WWW under http://dx.doi.org/10.1002/chem.201000458.

band center and ORR activity has been discussed extensively by Zhang et al.,[11,13] who established that there is a "volcano-type" relationship between the experimentally determined ORR activities and calculated binding energy for the Pt monolayer deposited on various single-crystal substrates (Pt_{ML}/M; M = Ru(0001), Ir(111), Rh(111), Au(111), Pd-(111)). Their results showed that the stronger or weaker binding energy of atomic oxygen at the various substrates cause a sluggish ORR reaction. Nørskov et al. proposed a correlation between the position of the d-band center relative to the Fermi level with the measured ORR activities of Pt_3M alloy system (M = Ni, Co, Fe, Ti).[15] The d-band structure, dioxygen dissociation, and the formation of oxygenated intermediates at the modified surface have been considered as crucial factors in understanding the oxygen reduction kinetics. Hence, it is of particular interest to understand how the electronic and geometric structure of these designed electrocatalysts can be manipulated.

A number of studies have focused on controlling the electron configuration and architecture of Pt-based bimetallic nanocatalysts by alloying platinum with various proportions of a second metal. Recently, we studied the modified d-band vacancies in bimetallic Pt–Ag/C nanoparticles synthesized by the ethylene glycol method with adjustment of pH of the reaction medium, and we were able to establish a relationship between the size effect and d-band vacancies.[16] Chen et al. demonstrated that ORR activity can be fine-tuned by optimizing the amount of Fe in Pt–Fe/C nanocatalysts.[17] The authors discovered a relationship between Fe content and ORR activity at the surface of synthesized Pt–Fe/C catalysts with various compositions, and found that Fe content influences the electron transport between adsorbed oxygen and the Pt sites, which can impact their ORR activity. Toda et al. examined the ORR activities of carbon-supported bimetallic catalysts (Pt–M/C, M = Fe, Ni, Co), and presented an enhanced mechanism for the ORR based on the observed d-band vacancies in the Pt alloy system.[18]

Although the Pt–Pd system is of great interest due to its enhanced stability in acidic environments, as well as its high selectivity for ORR in the presence of methanol,[19–21] there is a clear need for a study on the effect of the alloying extent and d-band vacancies on the reactivity of Pt_xPd_{1-x} nanoparticles in the ORR and methanol oxidation reaction (MOR). Herein, d-band vacancies and extent of alloying in the Pt_xPd_{1-x}/C nanocatalysts are manipulated by varying atomic composition. We found that the reactivity depends on the extent of alloying and d-band vacancies of the Pt_xPd_{1-x}/C nanocatalysts such that there is a synergistic effect on ORR activity and an antagonistic effect on MOR activity.

Results and Discussion

Figure 1 represents a typical powder X-ray diffraction (XRD) pattern obtained for the commercial catalysts and those prepared in our laboratory. The peak located at around 24° in all patterns arises from the (0002) hexagonal phase of Vulcan XC-72R carbon. The other four peaks are the characteristic peaks of the face centered cubic (FCC) crystalline structure of platinum. The peaks correspond to the planes (111), (200), (220), and (311) at 2θ of around 40, 48, 70, and 84°, respectively. These XRD patterns reveal that our catalysts are single-phase solid solutions. Compared with the plane (111) of JM 20 Pt/C, the diffraction peaks of our catalysts are shifted to higher angles, which indicates that the addition of Pd to Pt leads to a decrease in the lattice parameters of Pt_xPd_{1-x} alloy nanoparticles due to contraction of the unit cells.

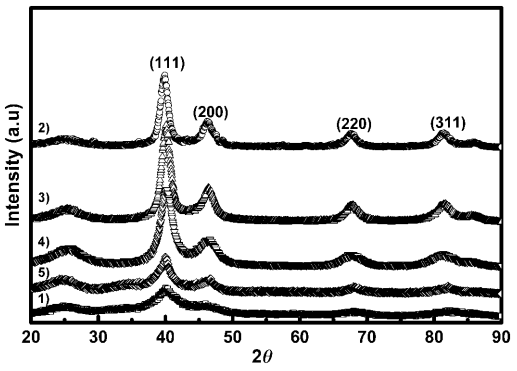

Figure 1. XRD patterns of commercial JM 20 Pt/C (line 1) and D-BASF Pd/C (line 5), and our synthesized Pt_xPd_{1-x}/C nanocatalysts (Pt_3Pd_1/C (line 2), Pt_1Pd_1/C (line 3), and Pt_1Pd_3/C (line 4)).

High-resolution TEM images of the commercial D-BASF Pd/C and JM 20 Pt/C are shown in Figure 2a and b, while the TEM images of our synthesized Pt_3Pd_1/C, Pt_1Pd_1/C, and Pt_1Pd_3/C are shown in Figure 2c, d, and e, respectively. As the figure shows, the metal clusters are well dispersed on the carbon support. The average grain size of each catalyst was calculated by using Scherrer's equation.[22] Particle diameters estimated from the TEM images are fairly consistent with the grain sizes calculated from the XRD patterns, as listed in Table 1.

Interestingly, the grain size decreases with increasing atomic ratio of Pd. During the synthesis, the palladium in the $PdCl_2/NH_4F$ complex was reduced to Pd^0 by accepting electrons released from the oxidation of $NaBH_4$. The reduction rate is inhibited by the stability of the Pd complex, and this subsequently avoids overgrowth of the nanoclusters.[23] Thus, the particle size of the nanocatalysts decreases with increasing concentration of Pd complex in the solution. The particles of Pt_1Pd_3/C are the smallest among the synthesized catalysts. The atomic compositions of our Pt_xPd_{1-x}/C nanocatalysts were determined by X-ray absorption spectroscopy (XAS). The results indicate that the Pt to Pd atomic ratio is close to the nominal values for the prepared Pt_xPd_{1-x}/C nanocatalysts.

Figure 3 represents the Fourier-transform extended X-ray absorption fine-structure spectroscopy (FT-EXAFS) spectra at the Pt L_{III} edge and Pd K edge, respectively. FT-EXAFS spectra provide structural information on nanocatalysts, in-

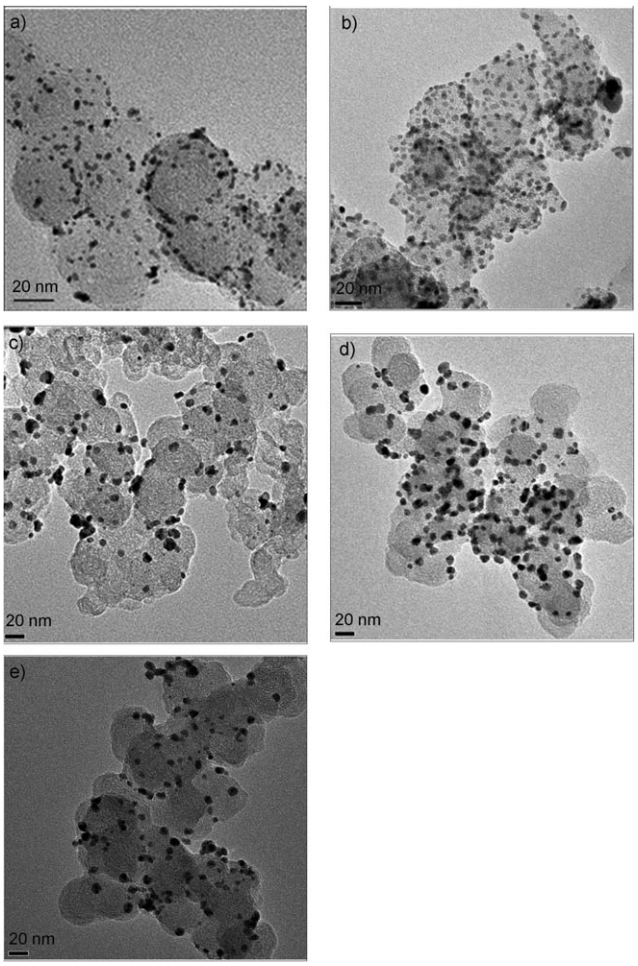

Figure 2. TEM images of a) JM20 Pt/C, b) D-BASF Pd/C, c) Pt_3Pd_1/C, d) Pt_1Pd_1/C, and e) Pt_1Pd_3/C.

Table 1. Bulk composition, particle size, and electrochemical surface area (ECSA) of the commercial JM 20 Pt/C, D-BASF Pd/C catalysts and our synthesized Pt_xPd_{1-x}/C nanocatalysts.

Sample	Particle diameter [nm] XRD	TEM	Atomic ratio [Pt/Pd] XAS [a]	ECSA [$m^2 g^{-1}$ Pt]
JM20 Pt/C	2.7	2.9	100:0	62.5
Pt_3Pd_1/C	5.3	5.7	75:25	51.3
Pt_1Pd_1/C	4.2	4.5	47:53	46.4
Pt_1Pd_3/C	3.3	4.0	23:77	37.6
D-BASF Pd/C	4.1	4.2	0:100	42.7

[a] Determined by the edge jump of Pt L_{III} edge and Pd K edge.

cluding atomic distance and coordination number. The samples were pretreated in a reduced atmosphere before the XAS measurements were performed, so that the presence of trace oxides could be completely excluded. The peaks appearing between 1.9 and 3.1 Å at the Pt L_{III} edge represent Pt–Pt and Pt–Pd coordination. At the Pd K edge, the peaks appearing between 1.9 and 3.2 Å represent the contributions from Pd–Pt and Pd–Pd coordination. The structural parameters were obtained by following the convergent fitting,[23] as shown in Table 2. The homometallic coordination numbers

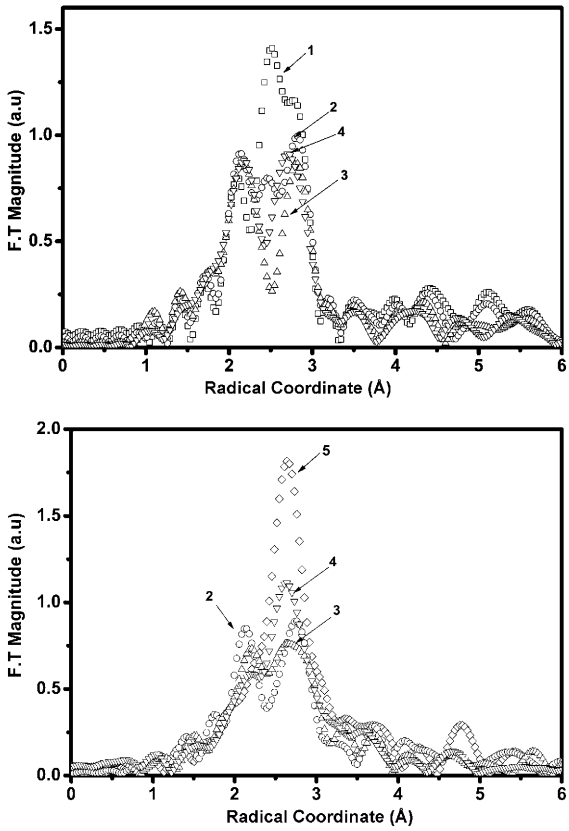

Figure 3. FT-EXAFS spectra at the Pt L_{III} edge(top) and at the Pd K edge (bottom) for JM 20 Pt/C (□), D-BASF Pd/C (◇), Pt_3Pd_1/C (○), Pt_1Pd_1/C (△), and Pt_1Pd_3/C (▽) nanoparticles.

N_{Pt-Pt} and N_{Pd-Pd} are greater for higher atomic ratios of Pt or Pd, respectively. The heterometallic coordination numbers (N_{Pt-Pd} and N_{Pd-Pt}) show the opposite trend. The various structural models will be discussed in detail with respect to the extracted coordination numbers in the following section.

Recently, we proposed various structural models based on the atomic distribution and extent of alloying in heterometallic nanoparticles.[24] The atomic distribution of Pt in the Pt_xPd_{1-x} cluster (labeled as P_{obsd}) is defined by the ratio of N_{Pt-Pd} to the total coordination numbers around the absorbing Pt ($P_{obsd} = N_{Pt-Pd}/(N_{Pt-Pd}+N_{Pt-Pt})$). Similarly, the atomic distribution of Pd in the Pt_xPd_{1-x} nanocluster (labeled as R_{obsd}) can be obtained from a similar relationship ($R_{obsd} = N_{Pd-Pt}/(N_{Pd-Pt}+N_{Pd-Pd})$). Once P_{obsd} and R_{obsd} are estimated, the extent of alloying of Pt (J_{Pt}) and Pd (J_{Pd}) can be estimated by Equations (1) and (2), respectively.[33]

$$J_{Pt} = P_{obsd}/P_{random} \times 100\,\% \quad (1)$$

$$J_{Pd} = R_{obsd}/R_{random} \times 100\,\% \quad (2)$$

The parameters P_{random} and R_{random} are the ratios calculated for perfectly alloyed bimetallic nanoparticles. They can be derived from the molar ratios of Pd and Pt in Pt–Pd bimetallic nanoparticles, as represented in Table 3.

Table 2. Best-fit parameters from the analysis at Pd K edge and Pt L_{III} edge EXAFS spectra of JM 20 Pt/C, Pt_xPd_{1-x}/C and D-BASF Pd/C nanocatalysts obtained from EXAFS fitting.

Sample	Shell	N[a]	R [Å][b]	ΔE_o [eV][c]	σ^2 [Å^2][d]	r factor
Pt_3Pd_1/C	Pt–Pt	7.44±0.18	2.762±0.001	6.826	0.006	0.0011
	Pt–Pd	2.31±0.10	2.764±0.002	2.127	0.008	
	Pd–Pd	2.62±0.16	2.775±0.003	1.039	0.006	
	Pd–Pt	7.12±0.10	2.764±0.002	−1.183	0.007	
Pt_1Pd_1/C	Pt–Pt	5.72±0.31	2.760±0.003	6.640	0.008	0.0034
	Pt–Pd	4.69±0.29	2.769±0.003	2.501	0.010	
	Pd–Pd	5.34±0.31	2.773±0.003	5.116	0.008	
	Pd–Pt	4.12±0.29	2.769±0.003	4.142	0.009	
Pt_1Pd_3/C	Pt–Pt	4.07±0.53	2.761±0.008	4.977	0.008	0.0058
	Pt–Pd	6.35±0.42	2.763±0.003	1.419	0.009	
	Pd–Pd	7.39±0.47	2.782±0.003	5.138	0.010	
	Pd–Pt	1.91±0.42	2.763±0.003	3.027	0.008	
D-BASF Pd/C	Pd–Pd	9.44±0.60	2.830±0.003	5.271	0.009	0.0083
JM 20 Pt/C	Pt–Pt	8.55±0.21	2.763±0.001	5.495	0.006	0.0009

[a] N = coordination numbers. [b] R_j = coordination distances. [c] σ_j^2 = mean squared disorder for the bond length. [d] ΔE_0 = inner potential correction.

Table 3. Alloying extent of Pt (J_{Pt}) and Pd (J_{Pd}) in synthesized Pt_xPd_{1-x}/C electrocatalysts derived from EXAFS structural parameters.

Sample	ΣN_{Pt-i}	ΣN_{Pd-i}	P_{obsd}	R_{obsd}	P_{random}	R_{random}	J_{Pt}	J_{Pd}
Pt_3Pd_1/C	9.75	9.74	0.237	0.731	0.245	0.755	96.71	96.84
Pt_1Pd_1/C	10.41	9.46	0.450	0.435	0.532	0.468	84.66	93.04
Pt_1Pd_3/C	10.42	9.30	0.610	0.205	0.775	0.225	78.66	91.20

In addition to total coordination numbers ΣN_{Pt-i} and ΣN_{Pd-i}, the structural parameters P_{obsd}, R_{obsd} as well as J_{Pt} and J_{Pd} can be deduced accordingly (see Table 3). In general, lower J_i (i = Pt or Pd) values signify higher homometallic coordination in the cluster rather than heterometallic coordination. There are a number of factors that affect the extent of alloying. Previous work has highlighted the kinetics (synthesis parameters),[16,17,25] while thermodynamic factors (e.g., lattice mismatch, bond-dissociation energy, and electronegativity) have been shown to dominate the atomic distribution in the nanoclusters.[27] As shown in Table 3, we found high extents of Pt and Pd alloying in all our synthetic Pt_xPd_{1-x}/C nanocatalysts. Low lattice mismatch between Pt and Pd facilitates atom deposition at the heterometallic surface, and thus, high extents of alloying in the Pt_xPd_{1-x}/C nanocatalysts are achieved ($J_{Pt} > 70$; $J_{Pd} > 90$).

According to our proposed model, the nanoparticles exhibit a $Pt_{rich\text{-}core}Pd_{rich\text{-}shell}$ structure, when $N_{Pt-i} > N_{Pd-i}$ and $J_{Pd} > J_{Pt}$ for the Pt_1Pd_1/C and Pt_1Pd_3/C nanocatalysts. There is similarity in the observed extent of alloying of Pt and Pd in Pt_3Pd_1/C ($J_{Pt} \approx J_{Pd}$), and the total coordination number of Pt (N_{Pt-i}) is equal to N_{Pd-i}, which suggests that the structure assumes a random alloying type. As mentioned in the discussion on the growth mechanism, the various atomic ratios alter the deposition rate of the heterometallic clusters as well as the atomic distribution. This tendency indicates that the various structural models of nanocatalyst can be systematically manipulated by varying the atomic ratio.

In XAS analysis, the region in the vicinity of the absorption edge (0–50 eV) is referred to X-ray absorption near-edge structure spectroscopy (XANES). This region provides information about the coordination environment, local symmetry, and density of states of the absorbing element. The sharp peak observed in the XANES spectrum is an absorption-threshold resonance, generally referred to as the "white line". It is attributed to electronic transitions from $2p_{3/2}$ (Pt L_{III} edge) to the unoccupied d states near or above the Fermi level. The intensity of the white line is sensitive to the electron occupancy of the absorbing valence shell.

Figure S1 (Supporting Information) shows the normalized XANES Pt L_{III}, L_{II} edge spectra of JM 20 Pt/C and our synthesized Pt_xPd_{1-x}/C nanocatalysts. The white-line intensities at the Pt L_{III}, L_{II} edge for all the Pt_xPd_{1-x}/C nanoparticles are lower than those for the commercial JM20 Pt/C catalyst. A method modified by Reifsnyder et al.,[29] which was originally developed by Mansour et al.,[30] is employed in this work to quantify the difference in white-line intensities between our synthetic Pt_xPd_{1-x}/C nanocatalysts and JM20 Pt/C. After subtracting the platinum foil data from the catalyst data, the resulting curves were numerically integrated between −10 and +14 eV relative to the Pt absorption edge for both the L_{II} (ΔA_2) and L_{III} (ΔA_3) edges. The fractional change in the total number of unfilled Pt d-band states compared with the reference platinum foil (f_d) can be estimated by using Equation (3) .

$$f_d = \frac{\sigma_3 \Delta A_3 + (1.11\sigma_2 \Delta A_2)}{\sigma_3 \Delta A_{3r} + (1.11\sigma_2 \Delta A_{2r})} \quad (3)$$

All the areas (A_{3s}, A_{2s}, A_{3r}, and A_{2r}) were normalized by multiplying by the X-ray absorption cross section (σ) at the respective edge jump. The ΔA_i ($i = 2$ or 3) values are defined as the differences in normalized area between samples and the reference foil. When the number of unfilled d-states in the reference material (h_{Tr}) is known (equal to 1.60),[31] the number of unfilled d-states in the sample (h_{Ts}) can be calculated using Equation (4). The corresponding values are listed in Table 4.

$$h_{Ts} = (1 + f_d) h_{Tr} \quad (4)$$

Previous work has highlighted the relationship between d-band structure and geometry, which are both tunable by alloying with various metals, by varying the atomic composition,[17,18] and by varying particle size.[32] The lower d-band vacancy is mainly attributed to d-band electron transfer from Pd atoms. The Pt d-band vacancies in the Pt_xPd_{1-x}/C decrease with decreasing atomic ratio of Pd. Thus, the

Table 4. Fractional change of unfilled Pt d state (f_d) and number of unfilled state (h_{Ts}) with respect to Pt foil of JM 20 Pt/C and synthesized Pt_xPd_{1-x}/C catalysts with various Pt to Pd ratios.

Sample	ΔA_2	ΔA_3	A_{3r}	A_{2r}	σ_3	σ_2	f_d	h_{Ts}
Pt foil			19.17	12.413				1.600
JM20	−1.044	0.221	19.17	12.413	1.285	0.59	−0.012	1.580
Pt_3Pd_1/C	−1.599	0.072	19.17	12.413	4.392	2.063	−0.029	1.552
Pt_1Pd_1/C	−0.206	−0.486	19.17	12.413	1.696	0.78	−0.023	1.562
Pt_1Pd_3/C	0.166	−0.558	19.17	12.413	1.34	0.62	−0.018	1.570

Pt_3Pd_1/C nanoparticles possesses the lowest d-band vacancies among all the nanocatalysts because they have the highest alloying extent ($J_{Pt}=96.71$; $J_{Pd}=96.84$). The observed tendencies indicate that extent of alloying mainly dominates Pt d-band vacancy. Higher extent of alloying represents higher heterometallic bonding around the absorbing atoms, thus more d-band electrons are transferred from neighboring Pd to Pt.

The cyclic voltammograms (CVs) of commercial JM 20 Pt/C, D-BASF Pd/C, and our synthesized Pt_xPd_{1-x}/C nanocatalysts are shown in Figure 4. The hydrogen-adsorption and

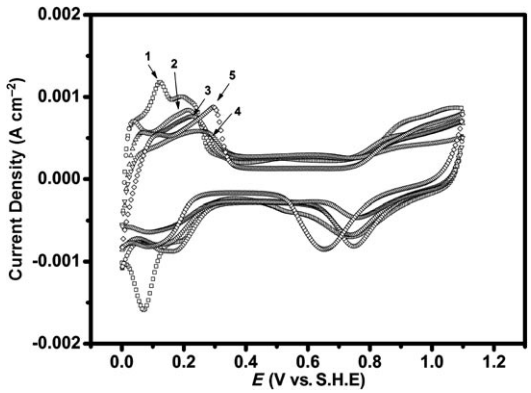

Figure 4. Cyclic voltammogram for JM 20 Pt/C (1), D-BASF Pd/C (5), Pt_3Pd_1/C (2), Pt_1Pd_1/C (3), and Pt_1Pd_3/C (4) nanoparticles in N_2-saturated sulfuric acid (0.5 M).

-desorption behavior of the Pt_xPd_{1-x}/C nanocatalysts is different from that observed for their monometallic counterparts. The Pt and Pd catalysts exhibit typical hydrogen adsorption/desorption characteristics.[34,35] The CV of D-BASF Pd/C reveals that the peak located at 0.29 V is characteristic of hydrogen desorption for polycrystalline Pd. Compared with JM 20, the peak position of hydrogen desorption for the Pt_xPd_{1-x}/C nanocatalysts is positively shifted along with an increase in the atomic ratio of Pd. The electrochemical surface area (ECSA) was determined by integrating the area of the hydrogen-desorption region after subtracting the background, as listed in Table 1.

Interestingly, the ECSA of the Pt_xPd_{1-x}/C nanocatalysts increases with size. Among the synthesized nanocatalysts, the smaller Pt_1Pd_3/C nanocatalysts adopt a $Pt_{rich\text{-}core}Pd_{rich\text{-}shell}$ structure. Since Pd is rich on the surface of the nanocatalyst, its ECSA is the lowest. The current at the oxide-formation region (0.7–0.9 V) for Pt_xPd_{1-x}/C decreases with increasing Pd content, which reveals that the addition of Pd inhibits the formation of oxygenated intermediates at the catalyst sites.[21]

The current density based on the mass-transfer correction for a rotating-disk electrode is obtained by using Equation (5), in which i is the experimentally obtained current, i_d refers to the measured diffusion-controlled current and i_k the kinetic current. Figure 5 shows that the kinetic current

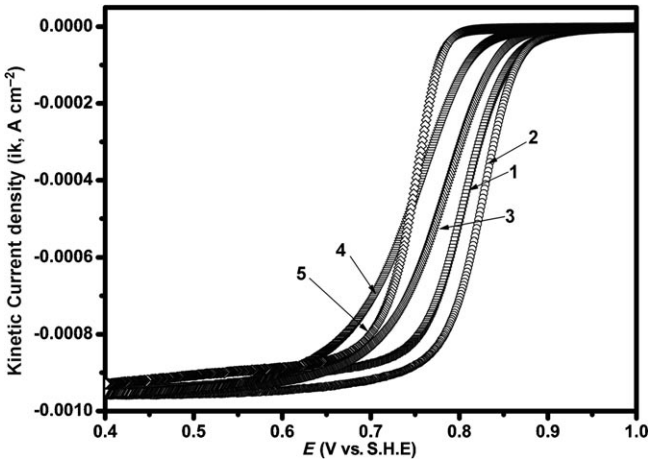

Figure 5. Hydrodynamic voltammogram for ORR at JM 20 Pt/C (1), D-BASF Pd/C (5), Pt_3Pd_1/C (2), Pt_1Pd_1/C (3), and Pt_1Pd_3/C (4) nanoparticles in O_2-saturated sulfuric acid (0.5 M).

and onset potential of ORR increase with Pt atomic ratio. Among the nanocatalysts, the Pt_3Pd_1/C nanocatalyst possesses the highest kinetic current and onset potential.

$$i_k = i_d i/(i_d - i) \quad (5)$$

The cyclic and hydrodynamic voltammograms of MOR are presented in Figures 6 and 7, respectively. Pd-containing nanoparticles exhibit poor MOR activities in terms of higher onset potential, and lower current density than JM

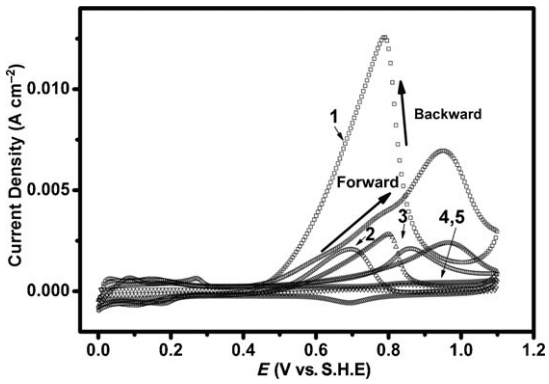

Figure 6. Cyclic voltammogram for JM 20 Pt/C (1), D-BASF Pd/C (5) Pt_3Pd_1/C (2), Pt_1Pd_1/C (3), and Pt_1Pd_3/C (4) nanoparticles in N_2-saturated methanol–sulfuric acid (1 M).

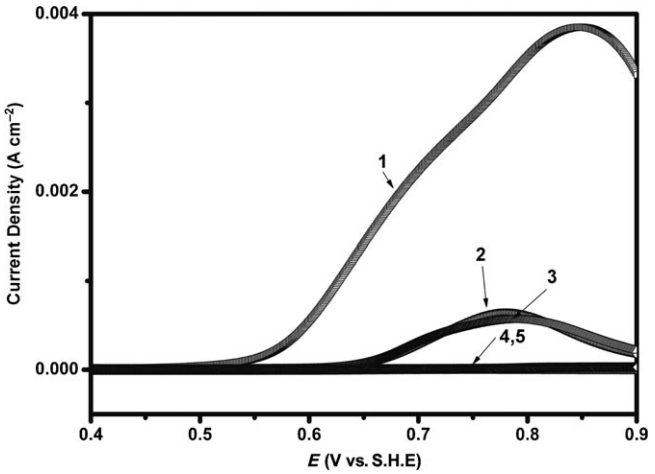

Figure 7. Hydrodynamic voltammogram for MOR at JM 20 Pt/C (1), D-BASF Pd/C (5) Pt_3Pd_1/C (2), Pt_1Pd_1/C (3), and Pt_1Pd_3/C (4) nanoparticles in N_2-saturated methanol–sulfuric acid (1 M).

20 Pt/C. Note that the current density decreases and onset potential shifts to more positive values with increasing Pd ratio. As previously discussed for the structural models, Pt_1Pd_3/C nanocatalysts, with their $Pt_{rich\text{-}core}Pd_{rich\text{-}shell}$ structure, lead to lower MOR activity and higher onset potential than the Pt_3Pd_1/C nanocatalysts. This can account for the weak adsorption of methanol on Pd and the weak ability to dehydrogenate methanol on Pd at low temperature.[36,37]

Figure 8 shows the variations in mass activities toward ORR and MOR with extent of alloying, and with Pt unfilled d state. The ORR activities show a systematic tendency towards Pt d-band vacancies and extent of alloying, so that the low Pt d-band vacancies and high extent of alloying in Pt_3Pd_1/C render it with the highest ORR activity among the nanocatalysts. The Pt_3Pd_1/C nanocatalyst enhances mass activity by 50% compared with the commercial JM 20 Pt/C.

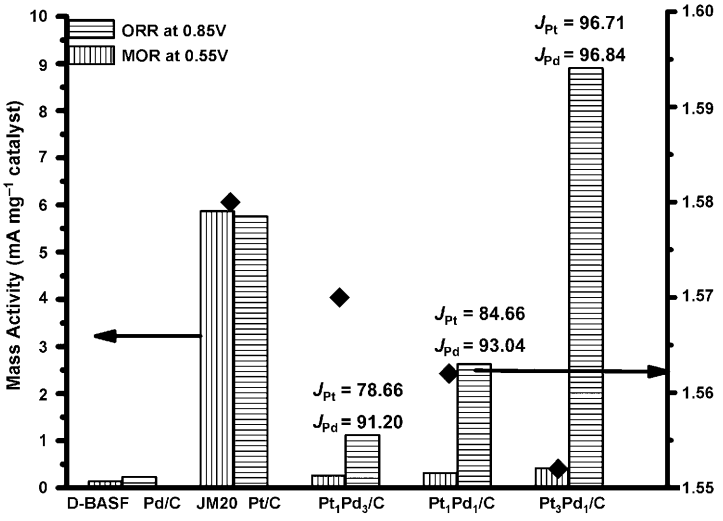

Figure 8. Hydrodynamic voltammogram for MOR at 0.55 V and ORR at 0.85 V at JM 20 Pt/C, D-BASF Pd/C and Pt_xPd_{1-x}/C nanoparticles with various Pt-to-Pd ratios in N_2-saturated methanol–sulfuric acid (1 M).

The CVs show that the presence of Pd in the Pt_xPd_{1-x}/C nanoparticles inhibits chemisorption of intermediates, and enhances ORR activity. However, too much Pd in the Pt_xPd_{1-x}/C nanoparticles (Pt_1Pd_1/C and Pt_1Pd_3/C) leads to low ORR activity. Higher d-band vacancies in the nanocatalysts have a negative effect on ORR activity by diminishing the electron transfer from the $2p$ orbital of O_2 to an empty $5d_{z^2}$ orbital of the surface Pt atom.[17] The Pt_1Pd_1/C and Pt_1Pd_3/C nanocatalysts with $Pt_{rich\text{-}core}Pd_{rich\text{-}shell}$ structure and excess Pt d-band vacancies are responsible for the weak dissociation of dioxygen. Overall, the Pt_3Pd_1/C nanocatalyst with the lowest Pt d-band vacancy represents an optimum electrocatalyst that exhibits the dual properties of high ORR activity and methanol tolerance.

Conclusion

Pt_xPd_{1-x}/C catalysts with various Pt to Pd ratios were examined for their electrocatalytic activities in ORR and MOR in acidic electrolyte, and were compared with the commercial nanocatalysts JM 20 Pt/C and D-BASF Pd/C. The atomic distribution and electronic structure of the synthesized Pt–Pd/C electrocatalysts were examined by XAS. It was found that the ORR activity strongly depends on the Pt d-band vacancies and extent of alloying. A decrease in Pt d-band vacancy facilitates O–O scission, and thus enhances ORR activity. Electrochemical studies revealed that the Pt_3Pd_1/C nanoparticles are the optimum nanocatalyst towards ORR, and possess remarkable methanol tolerance. Our results show that the Pt d-band vacancies and extent of alloying are tunable by varying the bulk composition. This opens up the possibility of fine-tuning the electrocatalytic activity of other alloy nanocatalysts.

Experimental Section

General: Reagent-grade chemicals were purchased from Acros and used as received without further purification. Pt_xPd_{1-x}/C nanocatalysts with various Pt/Pd atomic ratios ($x = 0.25$, 0.5, and 0.75) were synthesized by a boride reduction method: ammonium fluoride (125 mg), boric acid (625 mg), and appropriate amounts of $PdCl_2$ and $PtCl_4$ were dissolved in deionized water (50 mL). Pretreated Vulcan XC-72R carbon (400 mg) was added, and the mixture subjected to ultrasonication for 2 h. The pH of the reaction suspension was adjusted to within the range of 8–9 by adding concentrated aqueous ammonia solution. Finally, sodium borohydride solution (0.1 M) was slowly added dropwise with vigorous stirring at 25 °C. The catalyst powders were filtered and washed with distilled water. The obtained catalyst cakes were then dried in an oven at 60 °C for 6 h. The metal loading (Pt + Pd) was maintained at 20 wt% based on XC-72R for all our synthesized catalysts, in order to be comparable with the commercial catalysts JM 20 Pt/C and D-BASF Pd/C.

XRD and TEM measurements: XRD patterns of JM20 Pt/C, D-BASF Pd/C, and synthesized Pt_xPd_{1-x}/C nanocatalysts were performed by using a Rigaku Dmax-B X-ray diffractometer, Japan, with a $Cu_{K\alpha}$ radiation source operated at 40 kV and 100 mA. A scan rate of 0.05° s^{-1} for 2θ between 20 and 90° was used. The high-resolution TEM (HRTEM) images of Pt_xPd_{1-x}/C were obtained by using a Philips/FEI Tecnai 20G2 S-Twin TEM apparatus. Prior to the HRTEM measurements, the sample solution

was prepared by suspending the synthesized catalysts in absolute ethanol solution with ultrasonication. A drop of the sample specimen was applied onto the carbon-supported copper grid, which was placed in a vacuum oven overnight at 25 °C.

XAS measurements: Spectra were recorded at beam line 01C1, National Synchrotron Radiation Research Center, Taiwan. The electron-storage ring was operated at 1.5 GeV with a current of 300 mA. A Si (111) double-crystal monochromator was employed for the energy selection with resolution $\Delta E/E$ better than 2×10^{-4} at both the Pt L_{III}-edge (11,564 eV) and the Pd K edge (24,350 eV). All experiments on bimetallic nanoparticles were conducted in a purpose-made cell of stainless steel. One hole was made in the cell. After inserting the solid samples, the chamber was sealed with a screw to avoid exposure of the sample to the outer atmosphere. Before performing the XAS analysis, the sample was purged with He gas for 30 min to eliminate volatile compounds. Subsequently, it was reduced with 2% H_2 at room temperature for 1 h to remove oxides. The total amount of the sample was adjusted to reach the optimum absorption thickness ($\Delta\mu x = 1.0$; $\Delta\mu$ is the absorption edge and x is the thickness of the sample), so that proper edge jump could be achieved during the measurements. All spectra were recorded at room temperature in transmission mode. Higher harmonics were eliminated by detuning the double crystal Si (111) monochromator. Three gas-filled ionization chambers were used in series to measure the intensities of the incident beam (I_o), the beam transmitted by the sample (I_t), and the beam subsequently transmitted by the reference foil (I_r). The third ion chamber was used in conjunction with the reference sample, a Pt foil for the Pt L_{III} edge measurements and Pd foil for Pd K edge measurements. All measurements were compared against the reference samples. Control of parameters for EXAFS measurements, collection modes, processing of data, and calculation of errors were performed following the guidelines set by the Standards and Criteria Committee of the International XAFS Society.

XAS data analysis: The EXAFS function, χ, was obtained by subtracting the post-edge background from the overall absorption coefficient, and then normalizing to the edge jump. The normalized function, $\chi(E)$, was then converted to k space, which is the photoelectron wave vector. The wave-vector function $\chi(k)$ was weighted by k^2 to compensate for the damping of the backscattering oscillation in the high k region. Subsequently, k^2-weighted $\chi(k)$ data ranging from 3.20 to 12.45 $Å^{-1}$ at the Pt L_{III} edge and from 3.30 to 11.50 $Å^{-1}$ at the Pd K edge were converted to r space by Fourier transformation to indentify the backscattering contributions of each coordination shell. A nonlinear least-squares algorithm was employed to curve-fitting in the r space ranging from 1.65 to 3.31 Å at the Pt L_{III} edge and from 1.78 to 3.30 Å at the Pd K edge. The reference foil of Pt–Pd alloy was not available for the calibration. Hence, the effective scattering amplitude $f(k)$ and phase shift $\delta(k)$ of the Pt–Pd reference were modeled from the FEFF7 code by fixing the Pt atoms at (0,1/2,1/2,), (1/2,0,1/2,) and (1/2,1/2,0) and Pd atom at (0,0,0) in the unit cell of a cubic closed-packed model. The reference phase and amplitude of Pt–Pt and Pd–Pd absorbers were obtained from the Pt foil and Pd foil, respectively. All the computer programs were implemented in UWXAFS 3.0 package,[38] and the backscattering amplitude and phase shift of the specific-atom model were calculated by the FEFF7 code.[39] In this analysis, the structural parameters corresponding to first-shell coordination, such as coordination numbers (N), bond length (R), Debye–Waller factor (σ_j^2), and inner potential shift (ΔE_0), have been calculated. The amplitude reduction factor (S_0^2) represents the energy loss during multiple electron excitations. By fixing the values of coordination number in the FEFFIT input file, the obtained S_0^2 values were 0.95 and 0.905 for Pt and Pd, respectively.

Electrochemical test: A conventional three-electrode electrochemical cell was used for all electrochemical measurements. Pt foil and a saturated calomel electrode (SCE) were used as the counter and reference electrodes, respectively, and were powered by a potentiosat/galvanostat (Solartron 1480). All of the potentials in this work were referenced against the reversible hydrogen electrode (RHE), and all the measurements were carried out at (25±1) °C. Catalyst powder (7 mg) was ultrasonically suspended in a mixture of ethanol (absolute, 0.45 mL) and Nafion solution (5 wt%, 0.05 mL) for 2 h. Then, catalyst ink (7 μL, 19.6 μg catalyst) was micropipetted onto a glassy carbon electrode (GCE) surface (0.1964 cm^2) and dried at ambient temperature until a uniform thin film with a metal loading of 100 $\mu g\,cm^{-2}$ was formed. The working electrode was immersed in N_2-saturated sulfuric acid solution (0.5 M), and the potential was scanned from 0.05 to 1.0 V for 10 cycles at a scan rate of 50 $mV\,s^{-1}$. The Pt-based electrochemical surface area (ECSA) was determined by integrating the hydrogen adsorption area of the CV. The integrated area was divided by the scan rate (50 $mV\,s^{-1}$) and 210 $\mu C\,cm^{-2}$, which represented the charge required to oxidize a monolayer of H_2 adsorbed on the Pt (111) surface. The ORR currents for all the nanocatalysts were recorded in O_2-saturated sulfuric acid solution (0.5 M). The linear sweep was started from 1.0 to 0.4 V at a scan rate of 1 $mV\,s^{-1}$. The MOR currents for all the nanocatalysts were recorded in N_2-saturated methanol–sulfuric acid solution (1 M). The linear sweep started from 0.3 to 0.9 V at a scan rate of 1 $mV\,s^{-1}$ and the rotating speed was fixed at 1600 rpm.

Acknowledgements

The authors gratefully acknowledge financial support from the National Science Council (NSC-97-2120M-011-001 and NSC-97-2221-E-011-075-MY3), and facilities from the National Synchrotron Radiation Research Center (NSRRC), and the National Taiwan University of Science and Technology Taiwan.

[1] E. Reddington, A. Sapienza, B. Gurau, R. Viswanathan, S. Sarangapani, E. S. Smotkin, T. E. Mallouk, *Science* **1998**, *280*, 1735.
[2] T. Iwasita, F. C. Nart, *J. Electroanal. Chem.* **1991**, *317*, 291.
[3] T. R. Ralph, M. P. Hogarth, *Platinum Met. Rev.* **2002**, *46*, 3.
[4] M. T. Paffett, G. J. Beery, S. Gottesfeld, *J. Electrochem. Soc.* **1988**, *135*, 1431.
[5] P. S. Kauranen, E. Skou, *J. Electroanal. Chem.* **1996**, *408*, 189.
[6] X. Ren, S. Zelenay, S. Thomas, J. Davey, S. Gottesfeld, *J. Power Sources* **2000**, *86*, 111.
[7] B. Bittins-Cattaneo, S. Wasmus, W. Vielstich, *J. Appl. Electrochem.* **1993**, *23*, 625.
[8] D. Chu, S. Gilman, *J. Electrochem. Soc.* **1994**, *141*, 1770.
[9] A. Aricò, P. Creti, P. L. Antonucci, V. Antonucci, *Electrochem. Solid-State Lett.* **1999**, *1*, 66.
[10] J. K. Nørskov, J. Rossmeisi, A. Logadottir, L. Limdqvist, J. R. Kitchin, T. Bligaard, H. Jnsson, *J. Phys. Chem. B* **2004**, *108*, 17886.
[11] J. L. Zhang, M. B. Vukmirovic, Y. Xu, M. Mavrikakis, R. R. Adzic, *Angew. Chem.* **2005**, *117*, 2170; *Angew. Chem. Int. Ed.* **2005**, *44*, 2132.
[12] V. R. Stamenkovic, B. Fowler, B. S. Mun, G. F. Wang, P. Ross, C. A. Lucas, N. M. Markovic, *Science* **2007**, *315*, 493.
[13] F. H. B. Lima, J. Zhang, M. H. Shao, K. Sasaki, M. B. Vukmirovic, E. A. Ticianelli, R. R. Adzic, *J. Phys. Chem. C* **2007**, *111*, 404.
[14] S. Chen, W. Sheng, N. Yabuuchi, J. Ferreira, L. F. Allard, Y. S. Horn, *J. Phys. Chem. C* **2009**, *113*, 1109.
[15] V. Stamenkovic, B. S. Mun, K. J. J. Mayrhofer, P. N. Ross, N. M. Markovic, J. Rossmeisl, J. Greeley, J. K. Nørskov, *Angew. Chem.* **2006**, *118*, 2963; *Angew. Chem. Int. Ed.* **2006**, *45*, 2897.
[16] B. J. Hwang, Kumar S. M. S.; C. H. Chen, R. W. Chang, D. G. Liu, *J. F. Lee J. Phys. Chem. C* **2008**, *112*, 2370.
[17] W. Chen, J. Kim, Sun, S. Chen, *J. Phys. Chem. C* **2008**, *112*, 3891.
[18] T. Toda, H. Igarashi, H. Uchida, M. Watanabe, *J. Electrochem. Soc.* **1999**, *146*, 3750.
[19] H. Q. Li, Q. Xin, W. Z. Li, Z. Z. Zhou, H. H. Jiang, S. H. Yang, G. Q. Sun, *Chem. Commun.* **2004**, 2776.
[20] H. Li, G. Sun, N. Li, S. Sun, D. Su, Q. Xin, *J. Phys. Chem. C* **2007**, *111*, 5605.
[21] J. Zhang, Y. Mo, M. B. Vukirovic, R. Klie, K. Sasaki, R. R. Adzic, *J. Phys. Chem. B* **2004**, *108*, 10955.
[22] V. Radmilovic, H. A. Gasteiger, P. N. Ross, *J. Catal.* **1995**, *154*, 98.

[23] L. Zhang, T. Lu, J. Bao, Y. Tang, C. Li, *Electrochem. Commun.* **2006**, *8*, 1625.
[24] EXAFS measurement and controlled parameters: a) Guidelines for Data collection models http://ixs.iit.edu/subcommittee_reports/sc/sc00report.pdf. b) Guideline for error reporting: http://ixs.iit.edu/subcommittee_reports/sc/err-rep.pdf.
[25] B. J. Hwang, L. S. Sarma, J. M. Chen, C. H. Chen, S. C. Shih, G. R. Wang, D. G. Liu, J. F. Lee, M. T. Tang, *J. Am. Chem. Soc.* **2005**, *127*, 11140.
[26] M. R. Knecht, M. G. Weir, A. I. Frenkel, R. M. Crooks, *Chem. Mater.* **2008**, *20*, 1019.
[27] F. R. Fan, D. Y. Liu, Y. F. Wu, S. Duan, Z. X. Xie, Z. Y. Jing, Z. Q. Tian, *J. Am. Chem. Soc.* **2008**, *130*, 6949.
[28] M. Brown, R. E. Perierls, E. A. Stern, *Phys. Rev. B* **1977**, *15*, 738.
[29] S. N. Reifsnyder, M. M. Otten, D. E. Sayers, H. H. Lamb, *J. Phys. Chem. B* **1997**, *101*, 4972.
[30] A. N. Mansour, J. W. Cook, D. E. Sayers, *J. Phys. Chem.* **1984**, *88*, 2330.
[31] A. V. Ankudinov, A. I. Nesvizhskii, J. Rehr, *J. Synchrotron Radiat.* **2001**, *8*, 92.
[32] J. A. vanBokhoven, J. T. Miller, *J. Phys. Chem. C* **2007**, *111*, 9245.
[33] S. Mukerjee, J. Mcreen, *J. Electroanal. Chem.* **1998**, *448*, 163.
[34] M. Hara, U. Linke, T. Wandlowski, *Electrochim. Acta* **2007**, *52*, 5733.
[35] T. Frelink, W. Visscher, J. A. R. van Veen, *J. Electroanal. Chem.* **1995**, *382*, 65.
[36] R. Jiang, W. Guo, Li, M. Li, D. Fu, H. Shan, *J. Phys. Chem. C* **2009**, *113*, 4188–4197.
[37] L. Luo, M. Futamata, *Electrochem. Commun.***2006**, *8*, 231.
[38] E. A. Stern, M. Newville, B. Ravel, Y. Yacoby, D. Haskel, *Physica B+C* **1995**, *208–209*, 117–120.
[39] S. I. Zabinsky, J. J. Rehr, A. L. Anukodinov, R. C. Albers, M. Eller, *Phys. Rev. B* **1995**, *52*, 2995.

Received: February 21, 2010
Revised: June 4, 2010
Published online: August 5, 2010

